Journal of Non-Crystalline Solids 542 (2020) 120148

Contents lists available at ScienceDirect

Journal of Non-Crystalline Solids

journal homepage: www.elsevier.com/locate/jnoncrysol

Effect of particle size distribution on the sinter-crystallisation kinetics of a SiO_2–Al_2O_3–CaO–MgO–SrO glass-ceramic glaze

J.L. Amorós[a,b], E. Blasco[a,*], A. Moreno[a,b], N. Marín[c], C. Feliu[a,b]

[a] Instituto de Tecnología Cerámica – Asociación de Investigación de las Industrias Cerámicas
[b] Department of Chemical Engineering. Universitat Jaume I, Campus Universitario Riu Sec, 12006 Castellon, Spain
[c] Federal University of Sao Carlos, Graduate Program in Materials Science and Engineering, Av. Trab. São Carlense, 400 - Parque Arnold Schimidt, São Carlos - SP, 13566-590, Brazil

ARTICLE INFO

Keywords:
Sintering
Crystallisation
Glass-ceramics
Kinetics

ABSTRACT

Sinter-crystallisation kinetics of a glaze with an average particle size of 9.6μm, 4.0μm and 0.65μm, which devitrified anorthoclase and diopside, were studied by non-isothermal techniques. It was confirmed that the crystallisation kinetics could be described by the Johnson–Mehl–Avrami–Kolmogorov model, assuming the Avrami index and activation energy to be independent of particle size. To describe the sintering kinetics, a kinetic model was developed, based on the Johnson–Mehl–Avrami–Kolmogorov model, assuming the effect of temperature on the process rate to be the same as its effect on the inverse viscosity of the glass matrix, and introducing a correction that took into account the difference between the heating rate of the kiln and that of the test piece. The pre-exponential factor of the developed model was confirmed to be proportional to the inverse of glaze average particle size. Glaze sinterability was observed to increase as the heating rate rose and/or average particle size decreased.

1. Introduction

In a previous article [1], the sinter-crystallisation kinetics of a glaze based on the SiO_2–Al_2O_3–CaO–MgO–SrO system, as well as the microstructure of the glazes obtained at different maximum temperatures, were studied using non-isothermal methods. Previous in-house research had shown that, on a laboratory scale, this glaze yielded coatings with good mechanical and aesthetic properties. There is currently a clear trend towards applying glazes on ceramic substrates by inkjet technology, which has been widely implemented in ceramic tile decoration and requires much smaller particle sizes than those used in traditional glazing. However, no studies were found in the literature on the influence of glaze particle size, at average particle size distribution (PSD) values, d_{50}, which range from 0.5μm to 10μm, on glaze sinter-crystallisation kinetics and on resulting glaze microstructure. Such information is similarly scarce in the case of glass-ceramics, though glass-ceramics sinterability [2–3] has been shown to depend, in addition to their nature, on average particle size, d_{50}, and on the heating rate, a. This study examines the combined effect of these two variables (a and d_{50}) on the sinter-crystallisation kinetics of the above glaze [1] and on its resulting microstructure. The results obtained will also be applicable to the study of the sinterability of other glass-ceramic materials.

1.1. Determination of the kinetic parameters from constant-rate heating experiments

The following equation describes the kinetics of a process:

$$\frac{dX}{dt}=k(T)f(X) \tag{1}$$

where f(X) is the kinetic model, which expresses the influence of X (degree of conversion), and k(T) is the rate constant that is generally related to temperature by the Arrhenius equation for relatively short temperature ranges:

$$k(T)=A\exp\left(-\frac{E}{RT}\right) \tag{2}$$

where A is the pre-exponential factor, E is the process activation energy, and R is the universal gas constant.

If the process is developed at constant-rate heating, a, Eq. 1 and Eq. 2 yield:

$$\frac{dX}{dT}=\frac{A}{a}\exp\left(-\frac{E}{RT}\right)f(X) \tag{3}$$

Integrating and considering the Murray and White approximation

* Corresponding author.
E-mail address: encarna.blasco@itc.uji.es (E. Blasco).

https://doi.org/10.1016/j.jnoncrysol.2020.120148
Received 30 March 2020; Received in revised form 27 April 2020; Accepted 30 April 2020

[4], one obtains the integral form of the kinetic model, g(X), and its relation to temperature:

$$g(x)=\int_0^x \frac{dX}{f(X)} = \frac{A}{a}\int_0^T \exp\left(-\frac{E}{RT}\right)dT = \frac{ART^2}{aE}\exp\left(-\frac{E}{RT}\right) \quad (4)$$

i) Crystallisation kinetics

The Johnson–Mehl–Avrami–Kolmogorov (JMAK) model [5–6] has been used successfully to describe the surface crystallisation kinetics of the studied glaze [1]. The integral form of this model is:

$$g(X_C)=[-\ln(1-X_C)]^{1/n_C} \quad (5)$$

where n_C, the Avrami index, was found to be 3 [1]. This value is characteristic of the surface crystallisation of very fine particles.

From Eq. 4 and Eq. 5 one obtains:

$$X_C = 1 - \exp\left\{-\left[\frac{A}{a}\frac{RT^2}{E}\exp\left(-\frac{E}{RT}\right)\right]^{n_C}\right\} \quad (6)$$

The effect of particle size distribution, PSD, on n was determined by the Augis–Bennett [7] equation:

$$nC = \frac{2.5/FWHM}{E/RT_p^2} \quad (7)$$

where FWHM is the full width of the crystallisation peak at half maximum in the DTA curve.

The other kinetic parameters, E and A, were determined by applying the Kissinger–Akahira–Sunose (KAS) method [8], in some cases fitting the experimental values of X_C to Eq. 6. The KAS method is based on the isoconversional principle (i.e. at a constant degree of conversion, X_C, the process rate, dX_C/dT, depends only on temperature).

Rearranging terms and taking logarithms in Eq. 4, one obtains:

$$\ln\left(\frac{a}{T^2}\right) = \ln\frac{AR}{Eg(X_C)} - \frac{E}{RT} \quad (8)$$

Applying the isoconversional principle, Eq. 8 yields:

$$\ln\left(\frac{a}{T_X^2}\right) = \ln\frac{A_X R}{E_X g(X_C)_X} - \frac{E_X}{RT_X} \quad (9)$$

For a selected value of X_C, the value of E_X is determined from the slope obtained on plotting the values of $\ln(\frac{a}{T_X^2})$ versus those of $\frac{1}{T_X}$, A_X being the intercept and $g(X_C)_X$ the value of Eq. 6 at the selected value of X_C. T_X is usually evaluated at the crystallisation onset temperature, T_0, corresponding to phase formation onset ($X_C = 0.01$) [9], and the crystallisation peak temperature, T_p, (in this study, $X_C = 0.5 \pm 0.02$).

ii) Sintering kinetics

In previous studies, the effect of temperature on the constant rate of the process, k(T), was verified to be the same as its effect on the inverse of glass matrix viscosity [1, 10, 11]. Therefore, Eq. 2 can be replaced with:

$$k(T) = A^*\cdot\exp\left(-\frac{B}{T - T_{VFT}}\right) \quad (10)$$

where $B = 7100K$ and $T_{VFT} = 600K$ are the values of the Vogel–Fucher–Tamman (VFT) equation parameters for glass matrix viscosity and A* is the pre-exponential factor.

Substituting Eq. 10 for Eq. 2, taking into account that glaze sintering kinetics were also appropriately described by the JMAK model (Eq. 5) [1], and operating in an analogous manner to the form described above, Eq. 6 becomes:

$$X_S=1-\exp\left\{-\left[\frac{A^*}{a}\frac{(T-T_{VFT})^2}{B}\exp\left(-\frac{B}{(T-T_{VFT})}\right)\right]^{n_S}\right\} \quad (11)$$

To determine the effect of PSD on kinetic parameters, A* and n_S, the values of X_S of the experimental sintering curves, obtained at different heating rates, a, and different PSDs, were fitted to Eq. 11, using non-lineal regression.

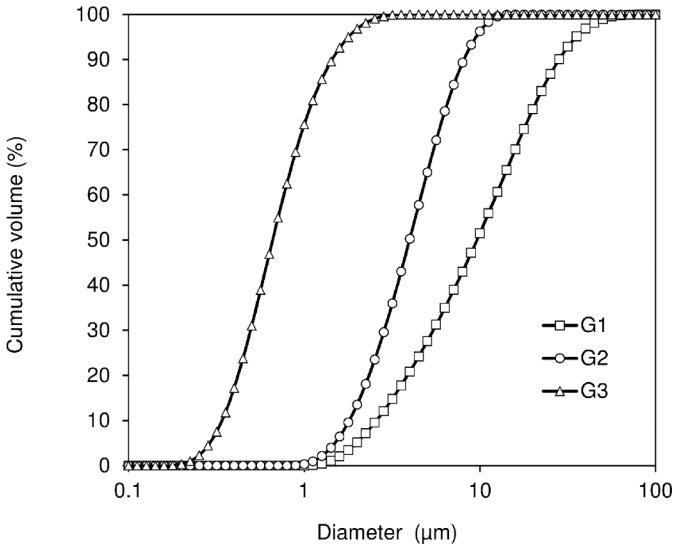

Figure 1. Particle size distributions of the studied glaze determined by laser diffraction.

2. Material and Methods

This study was performed with a glaze prepared by adding 8% kaolin by weight and the usual additives to a commercial frit composition based on the SiO_2–Al_2O_3–CaO–MgO–SrO system (these components make up more than 90 mol% of the frit), used and characterised in a previous study [1].

Aqueous suspensions of the above glaze (with 0.3% sodium carboxymethylcellulose and 0.1% sodium tripolyphosphate by weight), with a solids volume fraction of 0.65, were wet milled in a laboratory mill to two particle size distributions (PSDs), G1 and G2 (Figure 1). To obtain a finer PSD, an organic suspension, referenced G3 (Figure 1), was prepared at 45% by weight of previously dried particle size distribution G2, using isopropyl myristate as suspending agent and 3.5% of a copolymer as deflocculant. The G3 suspension was milled in two steps in a high-speed grinding mill, in the first step using zirconia balls of 1.3–1.7mm diameter and, in the second, using zirconia balls <0.3mm in diameter. The PSDs of the three glaze suspensions were determined by laser diffraction using the Fraunhofer theory. The following average particle sizes, d_{50}, were obtained for G1, G2, and G3, respectively: 9.6μm, 4.0μm, and 0.65μm.

Before the test pieces were formed, the aqueous glaze (G1 and G2) suspensions were dried at 110ºC, and the organic glaze (G3) suspension was calcined for 4h at 300ºC to remove the isopropyl myristate by oxidation.

Cylindrical test pieces, about 3mm in diameter and 5mm in height, were formed by filling a die with powder, compacting with a pressure-gauged push-rod, and extracting the sample onto an alumina plate. The sintering curves were determined from the initial, S_0, instantaneous, S, and minimum, S_{min}, silhouette surface areas of the test pieces by hot stage microscopy (HSM), at different heating rates (a = 2–50K/min). Diametral, $\varepsilon_d = \ln(d/d_0)$, and axial, $\varepsilon_h = \ln(h/h_0)$, strains were very similar until completion of sintering, as had been verified in a previous study [1].

Thus, assuming isotropic shrinkage, the sintering progress parameter, X_S, was calculated from:

$$Xs=\frac{\varepsilon_A}{\varepsilon_{A,max}} = \frac{\ln(S_0/S)}{\ln(S_0/S_{min})} \quad (12)$$

where ε_A and $\varepsilon_{A,\,max}$ are the instantaneous and maximum silhouette surface strain, respectively.

The estimated viscosity–temperature curve of a glass matrix with

the same composition as the glaze, expressed by the Vogel–Fucher–Tamman (VFT) equation, was determined in a previous study [1]:

$$\log\eta(\mathrm{Pa\hat{A}\cdot s}) = -5.67 + \frac{7100}{T(K) - 600} \quad (13)$$

To study the crystallisation process, the glaze DTA curves of the different PSDs (G1, G2, and G3) were determined at different heating rates (a = 2–50K/min), in air atmosphere. The crystallisation degree of conversion, X_C, at a given temperature is the ratio of the partial area at this temperature to the total area of the crystallisation exothermic peak [1].

The microstructure of the polished and platinum-coated test pieces was determined by scanning electron microscopy (SEM), at 10kV and high vacuum. The chemical composition of the crystals was determined by EDS, using the same procedure as in a previous study [1].

The goodness of each multiparameter fit was estimated by determining the variance, S^2:

$$S^2 = \frac{RSS}{m - p} \quad (14)$$

where m is the total number of experimental points used in the calculation, p is the number of fitting parameters, and RSS is the residual sum of squares:

$$RSS = \sum (y_{exp} - y_{cal})^2 = \min \quad (15)$$

where y_{exp} and y_{calc} are the experimental and calculated values, respectively, of the property to be fitted.

3. Results

3.1. Effect of particle size distribution (PSD) on the behaviour of the studied glass-ceramic glaze at 15K/min

The effect of particle size distribution, PSD, on sintering and crystallisation is plotted in Figure 2. The G2 glaze thermogram clearly shows the glass transition temperature, $T_g \approx 710$ºC, an exothermic peak of anorthoclase and diopside surface crystallisation at $T_p \approx 960$ºC, and the diopside endothermic melting peak, $T_m \approx 1165$ºC [1]. However, T_p rose significantly as average particle size, d_{50}, increased (plotted in Figure 5 and discussed below in Section 3.2), whereas T_m only rose slightly and T_g hardly varied as d_{50} increased.

Figure 2 shows that the experimental data of the degree of crystallisation, X_C, (empty symbols) and the corresponding crystallisation curves, $X_C(T)$, calculated from Eq. 6 with $n_C = 3$, $E_C = 340$kJ/mol, and values of A depending on the PSDs ($A = 9.50 \cdot 10^{11} s^{-1}$ for G1, $A = 1.25 \cdot 10^{12} s^{-1}$ for G2, and $A = 2.69 \cdot 10^{12} s^{-1}$ for G3), shifted towards lower temperatures as d_{50} decreased. It may be observed that the influence of particle size on crystallisation can be described by considering that only the pre-exponential factor, A, changed, without the other kinetic parameters (E_C and n_c) being modified, as was also subsequently confirmed.

The experimental values of the degree of sintering progress, X_S, (solid symbols) and its variation with temperature also shifted towards lower temperatures as d_{50} decreased. However, the quantitative influence of d_{50} on the sintering rate differed from that of d_{50} on crystallisation. Indeed, as d_{50} decreased, the degree of sintering increased before sintering was arrested by surface crystallisation. As Figure 2 shows, for G3 (the finest PSD) surface crystallisation began when sintering had been completed whereas, for G1, surface crystallisation occurred when densification had not yet been completed, $X_S \approx 0.95$. Therefore, d_{50} influenced glaze sinterability. It may furthermore be observed that the theoretical sintering curves, in which surface crystallisation was deemed not to occur, calculated from Eq. 11 with $n_S = 0.56$ and values of A* depending on the PSDs ($A^* = 2.0 \cdot 10^{10} s^{-1}$ for

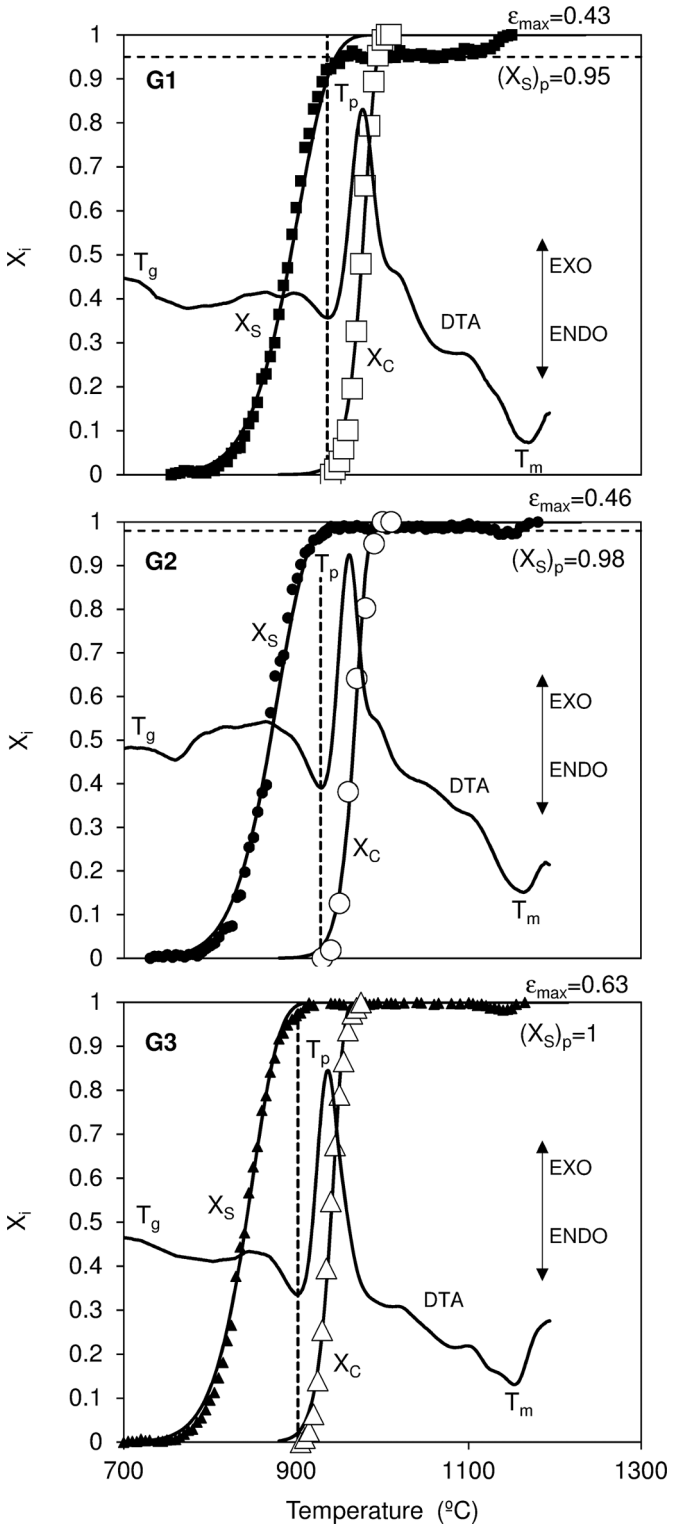

Figure 2. Effect of particle size distribution, PSD, on sintering and crystallisation. The solid and empty symbols are experimental data on sintering and crystallisation, respectively. The crystallisation curve was calculated from Eq. 6 with $n_C = 3$, $E_C = 340$KJ/mol, and $A = 9.50 \cdot 10^{11} s^{-1}$ for G1, $A = 1.25 \cdot 10^{12} s^{-1}$ for G2, and $A = 2.69 \cdot 10^{12} s^{-1}$ for G3. The sintering curve was calculated from Eq. 11 with $n_S = 0.56$, B = 7100K, $T_0 = 600$K, and $A^* = 2.0 \cdot 10^{10} s^{-1}$ for G1, $A^* = 9.5 \cdot 10^{10} s^{-1}$ for G2, and $A^* = 5.0 \cdot 10^{11} s^{-1}$ for G3. The dashed line is the temperature at crystallisation onset, T_0.

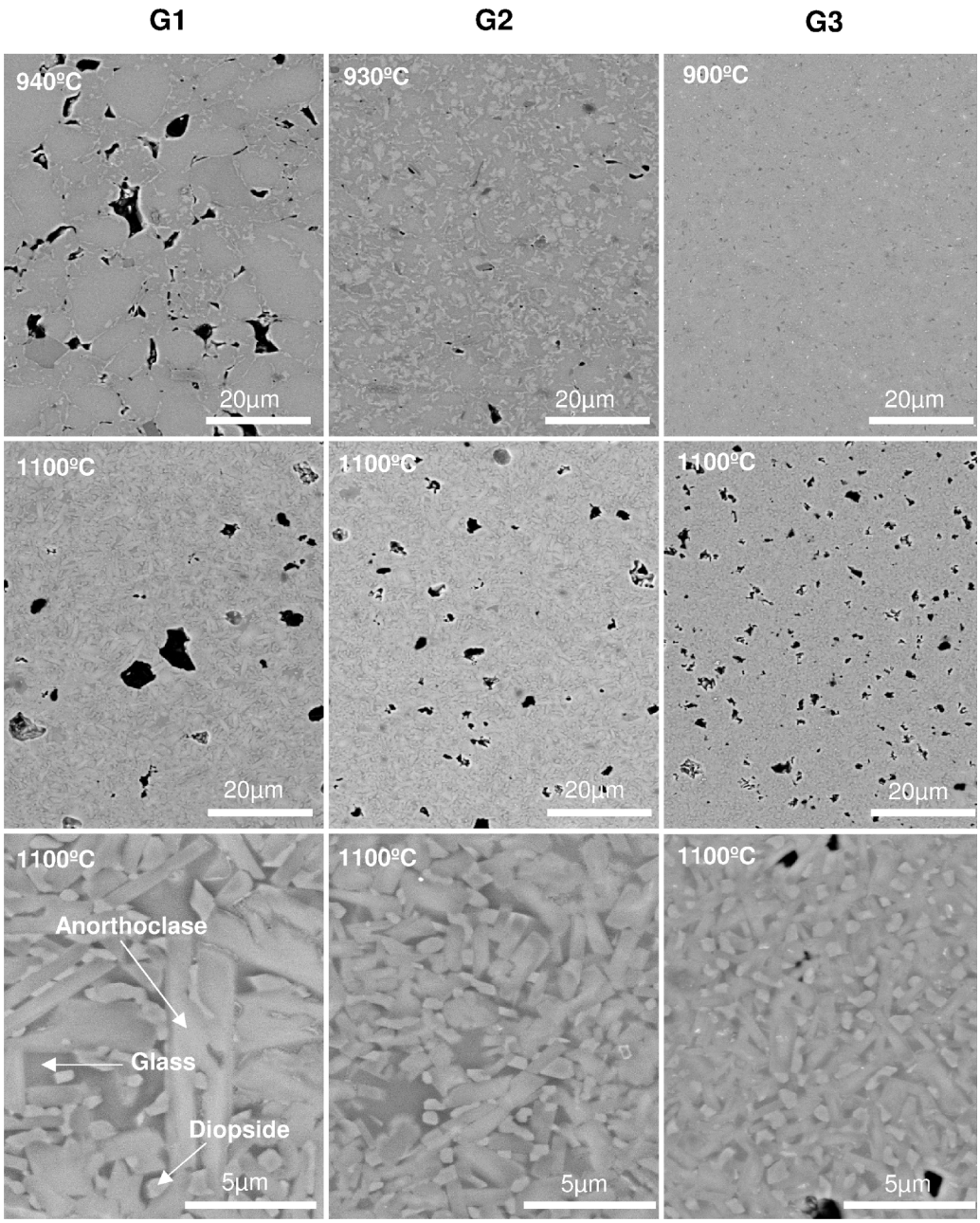

Figure 3. SEM micrographs of the studied glaze prepared from different PSDs and fired at different temperatures. Heating rate: a = 15K/min.

G1, $A^* = 9.5 \cdot 10^{10} s^{-1}$ for G2, and $A^* = 5.0 \cdot 10^{11} s^{-1}$ for G3), appropriately described this process up to the temperature at which the crystallisation process started (dashed line in Figure 2). It also shows that maximum silhouette surface strain, ε_{max}, increased as particle size decreased. This was mainly because, as the degree of milling increased, the compactness of the unfired test pieces decreased. This effect was much more pronounced on going from G2 to G3 than from G1 to G2 particle size distribution.

Observation of the microstructure of the test pieces corresponding to the three PSDs, each fired at the temperature at which sintering halted owing to crystallisation (Figure 3), revealed that intergrain porosity decreased in the order G1 > G2 > G3 ≈ 0, analogously to that of the degree of sintering progress at which sintering halted, $(X_S)_p$, in Figure 2 ($(X_S)_p = 0.95$ for G1, $(X_S)_p = 0.98$ for G2, and $(X_S)_p = 1$ for G3). In the case of G3 (Figure 4), in addition to the crystalline phases (anorthoclase/diopside) that began to form and the small quartz particles, also visible in G1 and G2 (Figure 3), the presence of zirconia particles

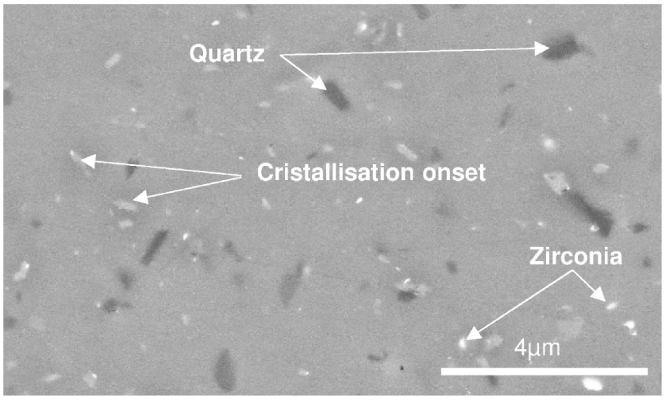

Figure 4. SEM micrograph of the G3 glaze fired at 900ºC. Heating rate: a = 15K/min.

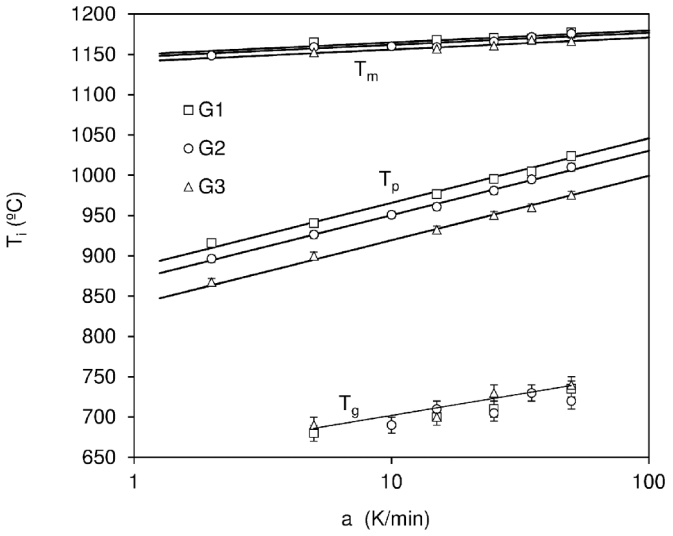

Figure 5. Combined effect of heating rate, a, and PSD on glaze melting peak temperature, T_m, crystallisation peak temperature, T_p, and glass transition temperature, T_g, (DTA). The error bars are the standard deviation of three measurements.

from the milling media and the practically complete absence of pores were verified. To be noted at 1100ºC (Figure 2), particularly for particle size distributions G2 and G3, was a rise in the number and size of the pores compared with those at crystallisation onset. This rise in porosity with temperature, with no change in firing shrinkage (Figure 2), was related to induced crystallisation pores, as reported in the literature [12–14] and verified for this glaze in a previous study [1]. It may furthermore be observed that, as glaze particle size decreased, pore and crystal (diopside/anorthoclase) size decreased, the number of crystals and pores increased, and the amount of glassy phase decreased. Thus, glaze particle size modified neither the sequence nor the nature of the crystallising phases, but only their size and amount.

3.2. Combined effect of heating rate, a, and particle size distribution (PSD) on crystallisation of the studied glass-ceramic glaze

The values of the glass transition temperature, T_g, crystallisation peak temperature, T_p, and melting peak temperature, T_m, were verified to decrease linearly with the logarithm of the heating rate, a, (Figure 5). For the sake of clarity, the values of the crystallisation onset temperature, T_0, which were very similar to those of T_p and also exhibited a similar trend to that of T_p, have not been plotted in this figure. However, the influence of the heating rate, a, slope of these curves, and particle size distribution, PSD, on each of these characteristic temperatures was different. To quantify this, the experimental data at each characteristic temperature were fitted, first, to relationships of the type T_i versus log(a), keeping the slope constant. The ordinate at the origin was then related linearly to the average particle size, d_{50}, of each PSD. The results of the fits are detailed in Table 1. The fits were good in all cases.

The results confirm that T_g did not depend on glaze PSD [15, 16]. The significant increase in the heat capacity of the glass at T_g, evidenced by an endothermic trend with the increase in temperature at DTA, from which T_g was determined, was closely related to the structural changes in the glass [17], which were independent of glaze PSD. In contrast, T_p and T_0 depended considerably on glaze average particle size, which implied surface crystallisation took place, as set out in a previous paper [1]. In accordance with this mechanism, as the specific surface area of the glass particles increases on milling, the number of surface nuclei and hence the rate of crystallisation rose [15, 18], this being evidenced in treatment at a constant heating rate by an advance

Table 1
Fitted equations that describe the influence of average particle size, d_{50} (μm), and heating rate, a (K/min), on glass transition temperature, T_g, crystallisation onset temperature, T_0, crystallisation peak temperature, T_p, and melting peak temperature, T_p. The table includes the values of the variance, S^2, of each fit.

Equation	S^2
T_g(ºC) = 53log(a) + 640	27.4
T_0(ºC) = 68log(a) + 31.5log(d_{50}) + 838	10.2
T_p(ºC) = 80log(a) + 40log(d_{50}) + 847	9.4
T_m(ºC) = 15log(a) + 7.53log(d_{50}) + 1142	7.98

of the crystallisation peak. Moreover, a considerable increase in T_g, T_0, and T_p and to a much lesser extent in T_m [1] was also confirmed with the rise in heating rate, since all these processes (glass transition, crystallisation, and crystal dissolution) are thermally activated.

3.2.1. Kinetic analysis

For each glaze particle size distribution (G1, G2, and G3), ln(a/T_0^2) was plotted versus 1/T_0 from the pairs of values (T_0, a) in order to obtain, in accordance with Eq. 9, from the slope of the straight line, the value of the crystallisation onset, E_0, activation energy at which X_C was assumed to be 0.01 (Table 2). The values of the activation energy corresponding to the crystallisation peak, E_p, were analogously calculated (Table 2). In this case, it was experimentally determined that, at crystallisation peak temperature, the degree of crystallisation progress, X_C, was 0.5 ± 0.02. On individually comparing the E_0 and E_p values of each glaze PSD, no significant differences were found as these differences were of the same order as the standard deviations of the E_0 and E_p values, only the value of E_p corresponding to PSD G1 being a little higher (about 7%) than that corresponding to PSD G2 and G3. On the other hand, in general, all the values of E_0, which were calculated at crystallisation onset (and at lower temperatures than those of crystallisation peak), were always slightly higher than those of E_p, (about 12% on average). This result is in agreement with the decrease in viscous flow activation energy with the rise in temperature [1, 9, 10].

The values of n_C for each PSD were calculated by the Augis–Bennett method (Eq. 7). To do so, the pairs of values (T_p, FWHM) were determined from the DTA crystallisation peak at each heating rate. Considering the value of E_p for each PSD (Table 2), the following results were obtained: $n_c = 2.8 \pm 0.4$ for G1, $n_c = 3.1 \pm 0.4$ for G2, and $n_c = 2.9 \pm 0.2$ for G3. The results indicate that, for the tested PSDs, average particle size did not affect the Avrami index, as the small variation of n_c observed was lower than the measurement standard deviation. As a result, $n_c = 3$ was used for each PSD. Furthermore, in view of the small random variation of crystallisation activation energy both at crystallisation onset, E_0, and at crystallisation peak, E_p, with average particle size (Table 2), it was considered the effect of glaze PSD on crystallisation could be suitably described by taking into account the effect of this variable on the pre-exponential factor, A_x. Indeed, on plotting ln(a/T_0^2) versus 1/T_0 (Figure 6) and ln(a/T_p^2) versus 1/T_p (Figure 7), keeping E_0 and E_p constant, very good results were obtained (Table 3). Using the values of the ordinates at the origin of these plots and those of $g(X_C)_0$ and $g(X_C)_p$, calculated from Eq. 5 (assuming $n_c = 3$), on applying Eq. 9, the values of the pre-exponential factors, A_0 and A_p, were obtained (Table 3).

The values of the pre-exponential factor, A_p, and of E_p were verified to correlate very well with the average diameter, d_{50}, of the glaze PSDs (Figure 8). The graph includes the values of A obtained on fitting the crystallisation curve corresponding to 15K/min to Eq. 6 (Figure 2). The values of A_p and A were observed to be very similar. In all cases, A_0, A_p, and A were proportional to $(1/d_{50})^{0.5}$.

Table 2
Values of the activation energy at crystallisation onset, T_0, and at crystallisation peak, T_p, for each studied PSD.

		G1	G2	G3
Crystallisation onset ($X_C = 0.01$)	E_0 (KJ/mol)	395 ± 14	384 ± 4	390 ± 13
	Int.* ($s^{-1} \cdot K^{-1}$)	23.3 ± 1.4	22.6 ± 0.4	24.1 ± 1.3
Crystallisation peak ($X_C = 0.5 \pm 0.02$)	E_p (KJ/mol)	365 ± 12	337 ± 6	341 ± 8
	Int.* ($s^{-1} \cdot K^{-1}$)	19.4 ± 1.1	17.2 ± 0.6	18.4 ± 0.8

(*) Value of the ordinate at the origin of the plot of Eq. 9.

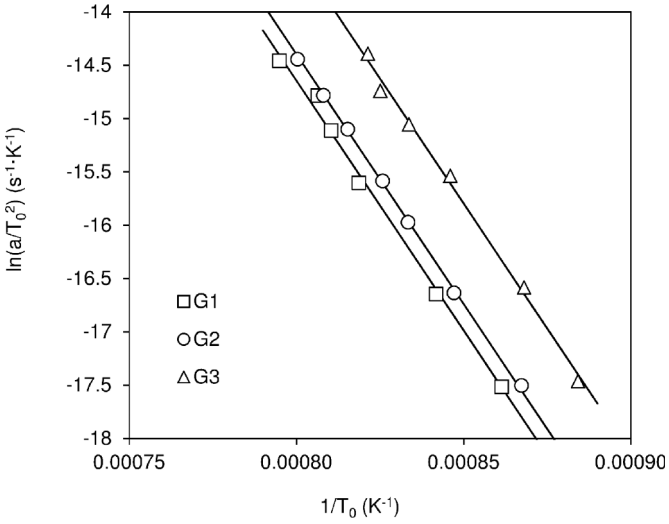

Figure 6. KAS plot of the effect of glaze PSD on crystallisation onset temperature, T_0.

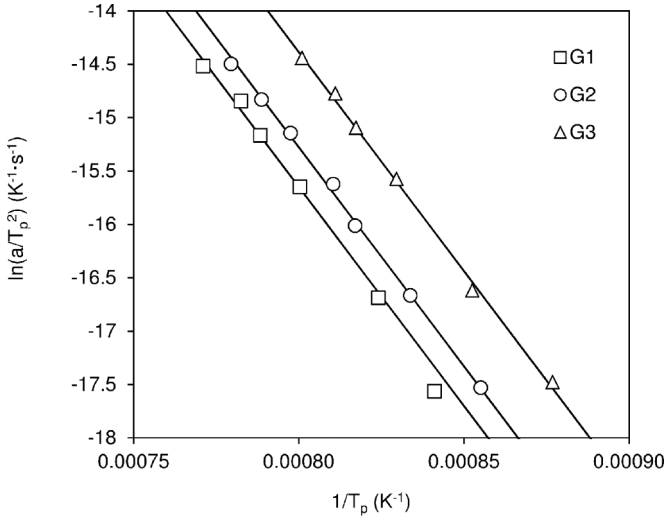

Figure 7. KAS plot of the effect of glaze PSD on crystallisation peak temperature, T_p.

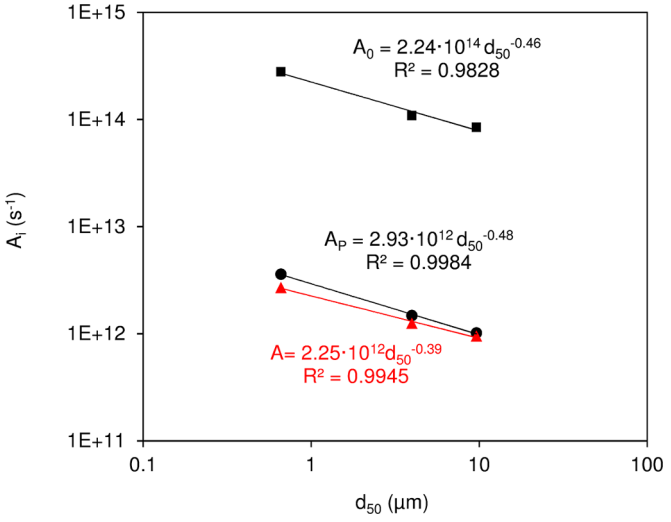

Figure 8. Influence of average particle size on the values of the pre-exponential factor corresponding to crystallisation onset, A_0, to crystallisation peak, A_p, and to the values resulting from the fit of the crystallisation curve to Eq. 6, A.

3.3. Combined effect of heating rate, a, and particle size distribution, PSD, on sintering of the studied glass-ceramic glaze

Glaze PSD considerably influenced the sintering curves, $X_S(T)$, obtained at different heating rates (Figure 9). However, its influence was much more pronounced at low heating rates, as the lower the heating rate and larger the particle size, the more did the sintering and crystallisation processes overlap. This led the degree of sintering at which sintering halted to decrease as the heating rate decreased and/or particle size increased.

3.3.1. Kinetic analysis

The sintering curves of each glaze PSD, for values of $X_S < (X_S)_p$, were fitted to Eq. 11 with the values of B and T_0 corresponding to the VFT equation (Eq. 10) and $n_S = 0.56$ (parameters already obtained and used elsewhere for glaze G2 [1]), and the values of A* depending on average particle size (Table 4). On plotting the curves resulting from these fits, however, the experimental curves were observed to depart from the calculated curves in a clear trend according to the heating rate, a, as the value of A* used for each PSD was the average value. However, the real rate at which the specimen was heated was always lower than the

Table 3
Values of the kinetic parameters at crystallisation onset (A_0 and E_0) and at crystallisation peak (A_p and E_p) and of the variance, S^2, of the fits.

		G1	G2	G3
Crystallisation onset ($X_C = 0.01$)	E_0 (kJ/mol)		390	
	A_0 (s^{-1})	8.5E+13	1.1E+14	2.8E+14
	S^2	9.5E-03	1.3E-03	7.5E-03
Crystallisation peak ($X_C = 0.5 \pm 0.02$)	E_p (kJ/mol)		341	
	A_p (s^{-1})	1.0E+12	1.5E+12	3.6E+12
	S^2	1.7E-02	3.2E-03	3.7E-03

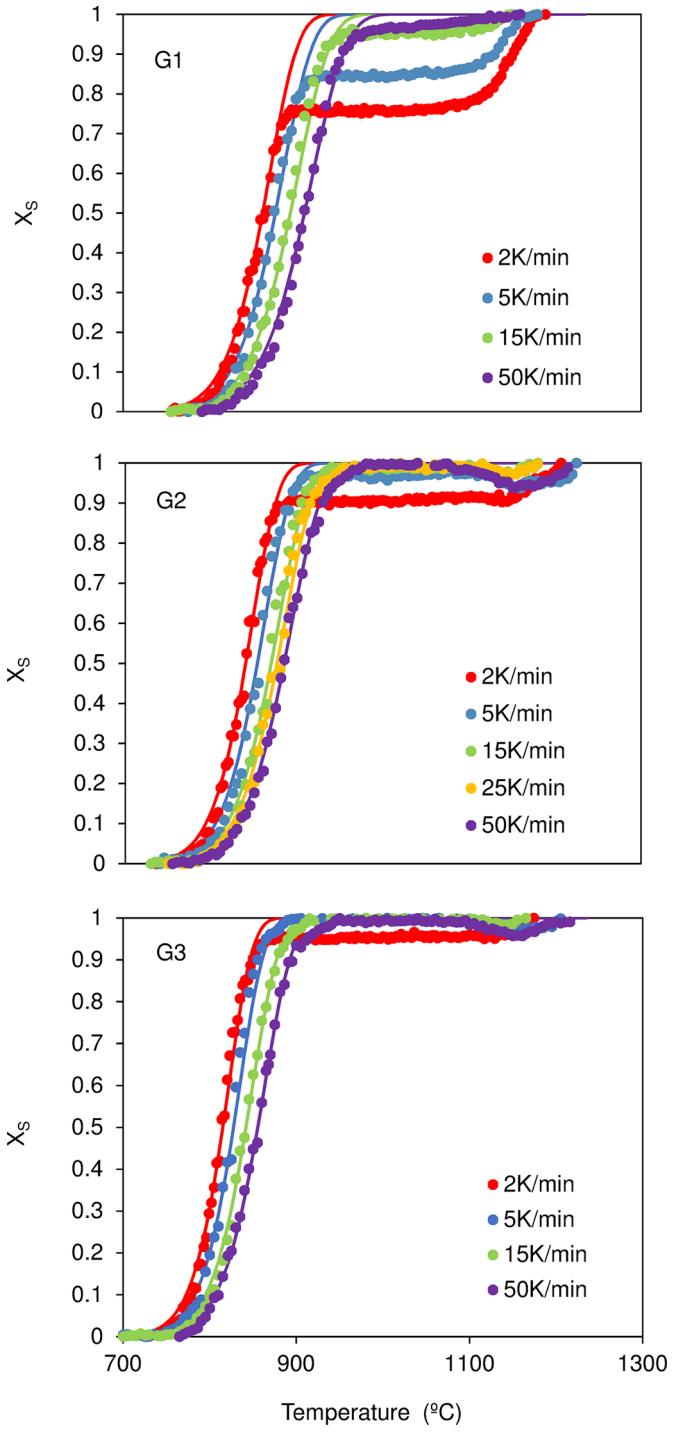

Figure 9. Combined effect of heating rate, a, and particle size distribution, PSD, on the sintering curves. The symbols are experimental data and the solid lines correspond to the values calculated from the model (Eq. 17).

programmed heating rate, a, and this difference increased as the heating rate, a, rose [19]. In order to obtain an empirical relationship that corrected this effect, first, for each PSD, the values of A* obtained from the fits for each heating rate, a, were plotted versus this variable (Figure 10). The results fitted straight lines whose slope and ordinate at the origin increased as A* did. In view of this, the values of A* were fitted to the equation:

$$A^* = k_s \cdot (1 + \kappa a) \quad (16)$$

where k_S is the pre-exponential factor when the heating rate tends to zero and κ is a fitting parameter that depends on the thermal properties of the material, test piece size, and kiln configuration and must, therefore, be independent of glaze PSD. The fit was verified to be excellent (Figure 11) with a fixed κ and a value of k_S for each PSD (Table 4). Introducing Eq. 16 into Eq. 11 yielded:

Table 4
Values of the kinetic parameters corresponding to Eq. 11 and Eq. 17 and of the variance, S^2, of the fits.

PSD	Eq.	A* (s^{-1})	n_S	T_{VFT} (K)	B (K)	No. of data	S^2
G1	11	2.00E+10	0.56	600	7100	139	1.63E-03
G2		9.50E+10				240	1.43E-03
G3		5.00E+11				192	1.03E-03

PSD	Eq.	κ (min/K)	K_S (s^{-1})	n_S	T_{VFT} (K)	B (K)	No. of data	S^2
G1	17	1.38E-02	1.88E+10	0.56	600	7100	139	6.38E-04
G2			7.33E+10				240	9.97E-04
G3			4.15E+11				192	7.08E-04

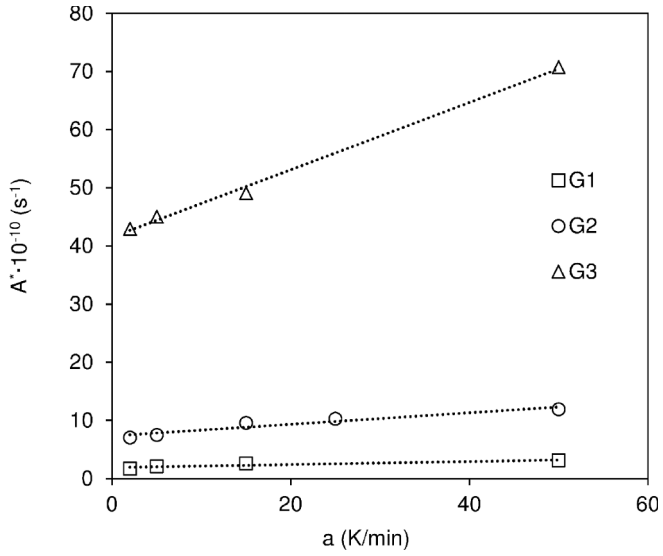

Figure 10. Influence of heating rate, a, on A* for each glaze PSD.

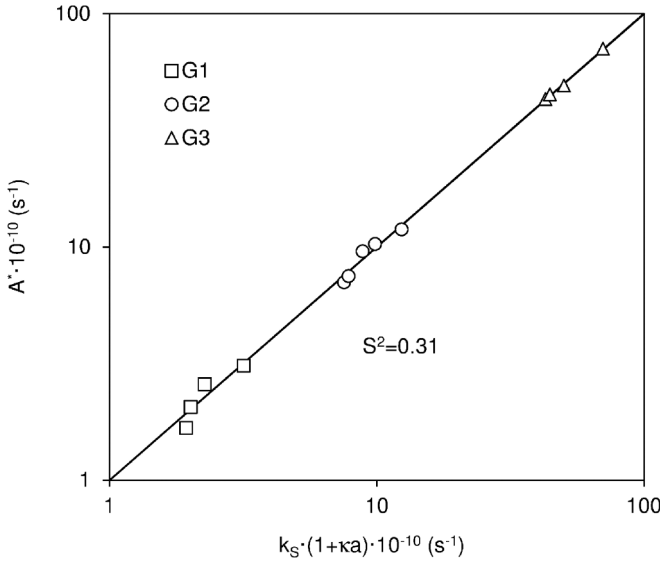

Figure 11. Comparison of the values of A* obtained from the fit of the sintering curves to Eq. 11 and the values calculated from Eq. 16.

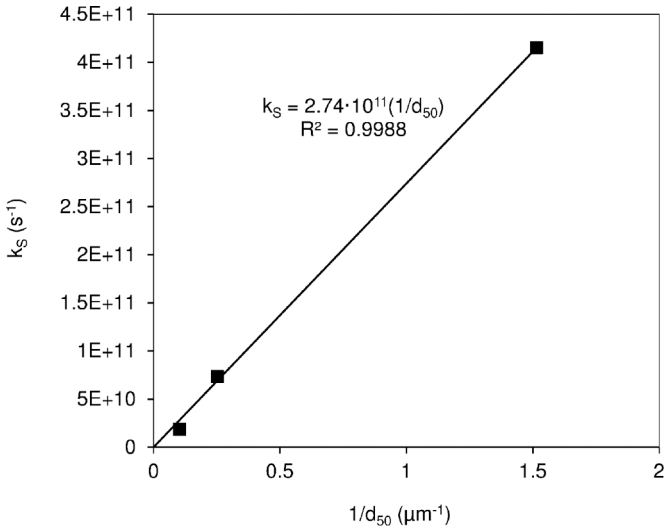

Figure 12. Influence of average particle size, d_{50}, on kinetic parameter k_s of Eq. 17.

$$X_S = 1 - \exp\left\{-\left[\frac{k_s \cdot (1+\kappa a)}{a}\frac{(T-T_{VFT})^2}{B}\exp\left(-\frac{B}{(T-T_{VFT})}\right)\right]^{ns}\right\} \quad (17)$$

Using the values of Table 4, the theoretical sintering curves were determined (Figure 9). This model described better than Eq. 11 (albeit appropriate) the influence of the heating rate and glaze PSD on the sintering process, using only two empirical fitting parameters: κ and k_S. Though this model (Eq. 17) is the same as the previous one (Eq. 11), it features two improvements. On the one hand, the kiln heating rate, a, was replaced with the rate at which the test piece was heated, a/(1 + κa). On the other, the average pre-exponential factor, A*, was replaced with k_s, the pre-exponential factor obtained on assuming that the heating rate tended to zero. Under these circumstances, the temperature was assumed to be uniform in the test piece and identical to kiln temperature.

The pre-exponential factor k_s was verified to be proportional to the inverse of average particle size, d_{50} (Figure 12). These results are consistent with the theoretical models of glass sintering [20–22], which predict that the sintering rate constant depends on the inverse of average particle size.

3.4. Sinterability of the studied glass-ceramic glaze: combined effect of sintering and crystallisation

In accordance with the literature [3, 23] and the results obtained in the previous sections, in this study sinterability, S, is defined as the difference between the temperature at which the sintering process would have been practically completed ($X_S = 0.99$) in the absence of crystallisation, T_S, and the experimental temperature of crystallisation onset, T_0. To calculate the values of T_S, corresponding to each PSD and heating rate, the pairs of values (X_S, T) were fitted for $X_S < (X_S)_p$ to Eq. 11, keeping B = 7100K, T_{VFT} = 600K, and $n_c = 3$ constant. In accordance with this definition, when S < 0, sintering halted before it was completed. In contrast, when S > 0, crystallisation began after sintering had been completed.

Glaze sinterability, S, (Figure 13) was observed to increase with the logarithm of the heating rate, log(a), this effect being independent of PSD (the slope of the straight lines remained constant). In addition, S decreased exponentially as average particle size increased. The results fitted the following equation very well:

$$S = 27.9\log(a) - 17.8\exp(0.097 d_{50}) \quad (S^2 = 2.72) \quad (18)$$

To clearly visualise the combined effect of glaze average particle size, d_{50}, and heating rate, a, on glaze sinterability, S, Figure 14 shows the isosinterability curves, calculated as a function of these variables, in accordance with the fitted equation of Figure 13. The coloured area in Figure 14 indicates the pairs of values of the heating rate and average PSD at which glaze sintering was completed (crystallisation began after sintering had been completed). Figure 14 also includes the experimental data of glaze sinterability (red squares). The fit of the experimental data and the calculated values of S is very good, if it is taken into account that the standard deviation of S was, in the most favourable cases, ± 2ºC.

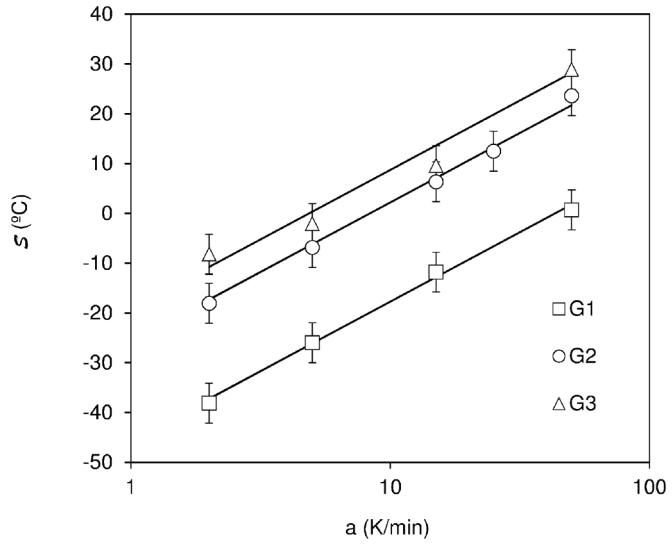

Figure 13. Influence of heating rate, a, and glaze PSD on glaze sinterability, S.

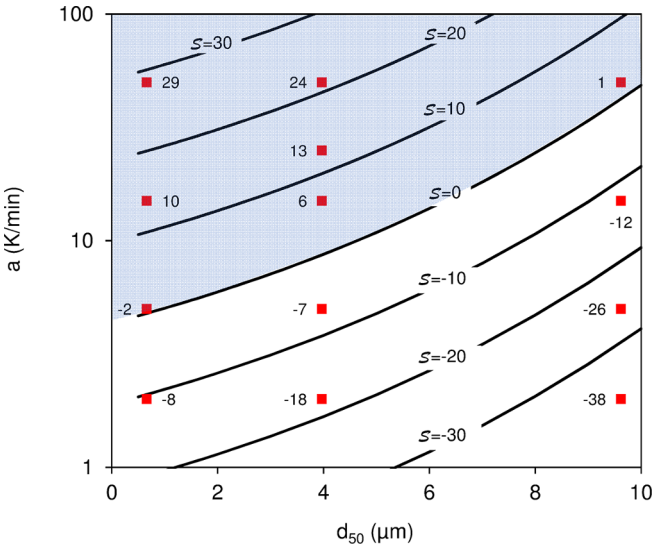

Figure 14. Experimental data (red squares) and contour map of glaze sinterability for a broad range of heating rates, a, and d_{50} of the studied PSDs.

On plotting the values of glaze degree of sintering progress at which sintering halted owing to surface crystallisation, $(X_S)_p$, versus glaze sinterability, S, (Figure 15), the results fitted the following equations:

$$\text{For } S \le 0 \quad (X_S)_p = 1 + 0.006S \quad (S^2 = 3.4 \cdot 10^{-4}) \quad (19)$$

and

$$\text{For } S \ge 0 \quad (X_S)_p = 1 \quad (20)$$

Assuming that glaze final porosity must increase as the degree of sintering progress at which sintering halts, $(X_S)_p$, decreases, it will be readily understood that the defined sinterability parameter, S, is very

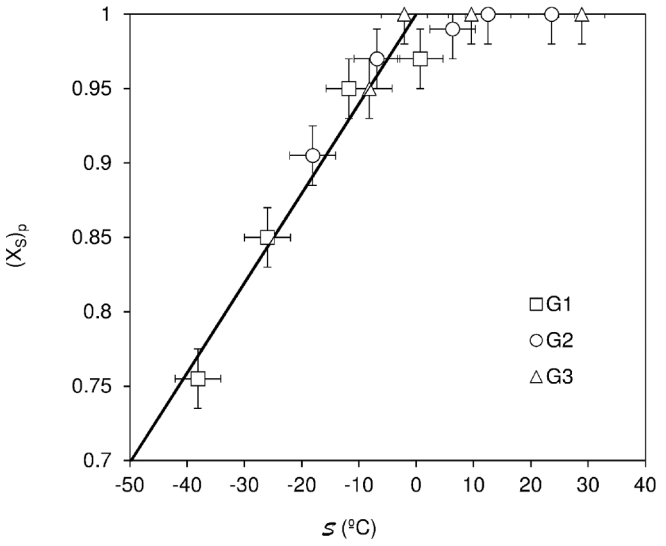

Figure 15. Relationship between the degree of sintering progress at which sintering halted owing to glaze crystallisation, $(X_S)_p$, and glaze sinterability, S.

useful when it comes to establishing the required operating variables for obtaining glazes with high crystalline phase content and low porosity.

4. Conclusions

The sinter-crystallisation kinetics of a glaze based on the system SiO_2–Al_2O_3–CaO–MgO–SrO, which devitrified anorthoclase and diopside, with average particle size distributions of 9.6μm, 4.0μm, and 0.65μm, were studied by non-isothermal techniques. It was verified that, for this range of particle sizes, the crystallisation kinetics were appropriately described by the JMAK model, keeping the Avrami index, $n_c = 3$, and the process activation energy, $E_C = 340$KJ/mol, constant and assuming that the pre-exponential factor depended on glaze average particle size, d_{50}.

To describe the sintering kinetics, a model was developed, based on the JMAK model, assuming the effect of temperature on the process rate to be the inverse of its effect on glass matrix viscosity. A correction factor to the kiln heating rate was introduced, which substantially improved the results, the factor being based on test piece heating rate always being lower than the programmed heating rate. The pre-exponential factor of the model under these conditions was verified to be proportional to the inverse of glaze average particle size, d_{50}.

Intergrain porosity of the glaze fired at the crystallisation onset temperature decreased as glaze average particle size, d_{50}, decreased, cancelling out at the finest d_{50}. Moreover, for the three studied glaze PSDs, in the glaze fired at its firing temperature, the presence of induced crystallisation porosity was confirmed. As glaze average particle size, d_{50}, decreased, the number of these pores increased, and pore size decreased. The same occurred with the number and size of the crystals.

There was observed to be a direct relationship between the degree of sintering progress at which sintering halted (owing to crystallisation) and glaze sinterability, S. Glaze sinterability, S, (defined as the difference between the temperature at which glaze densification would have been completed in the absence of crystallisation and the crystallisation onset temperature) increased as the heating rate rose and decreased as average particle size increased. A relationship was obtained that describes very well the combined influence of the heating rate and glaze average particle size on glaze sinterability.

CRediT authorship contribution statement

J.L. Amorós: Conceptualization, Methodology, Formal analysis, Writing - original draft, Writing - review & editing, Supervision. **E. Blasco:** Conceptualization, Methodology, Formal analysis, Writing - original draft, Writing - review & editing, Visualization, Supervision. **A. Moreno:** Conceptualization, Resources, Data curation, Supervision, Project administration, Funding acquisition. **N. Marín:** Software, Validation, Investigation, Data curation. **C. Feliu:** Resources, Data curation, Supervision, Project administration, Funding acquisition.

Declaration of Competing Interest

The authors declare that they have no known competing financial interests or personal relationships that could have appeared to influence the work reported in this paper.

Acknowledgements

This study was co-funded by the ERDF Operational Programme for the Valencia Region and by the Valencian Institute for Business Competitiveness (IVACE).

References

[1] J.L. Amorós, E. Blasco, A. Moreno, N. Marín, C. Feliu, C., Sinter-crystallisation kinetics of a SiO2–Al2O3–CaO–MgO–SrO glass-ceramic glaze, J. Non-Cryst. Solids. 532 (2020) 119900.
[2] R. Müller, On the kinetics of sintering and crystallization of glass powders, Glastech. Ber. -Glass Sci, Technol 67C (1994) 93–98.
[3] M.O. Prado, M.L.F. Nascimento, E.D. Zanotto, On the sinterability of crystallizing glass powders, J. Non-Cryst. Solids. 354 (2008) 4589–4597.
[4] P. Murray, J. White, Kinetics of the thermal dehydration of clays. Part IV. Interpretation of the differential thermal analysis of the clay minerals, Trans. Br. Ceram. Soc. 54 (1995) 204–264.
[5] M. Avrami, Kinetics of phase change. I. General theory, J. Chem. Phys. 12 (7) (1939) 1103–1112.
[6] M. Avrami, Kinetics of phase change. II. Transformation–time relations for random distribution of nuclei, J. Chem. Phys. 2 (8) (1940) 212–224.
[7] J.A. Augis, J.E. Bennett, Calculation of the Avrami parameters for heterogeneous solid-state reactions using a modification of the Kissinger method, J. Therm. Anal. 2 (13) (1978) 283–292.
[8] T. Akahira, T. Sunose, Method of determining activation deterioration constant of electrical insulating materials, Res Rep Chiba Inst Technol (Sci Technol) 16 (1971) 22–31.
[9] A. Karamanov, M. Pelino, Sinter-crystallization in the diopside–albite system: Part II. Kinetics of crystallization and sintering, J. Eur. Ceram. Soc. 26 (2006) 2519–2526.
[10] J.L. Amorós, E. Blasco, A. Moreno, E. Zumaquero, C. Feliu, Non-isothermal sintering of powdered vitrified composites. A kinetic model, Mater. Lett. 236 (2019) 236–239.
[11] E. Blasco, Sinterización de compactos de vidrio y composites vidrio-circón. Mecanismo y cinética del proceso. PhD Dissertation. Universitat Jaume I. Department of Chemical Engineering, Castellón (2017).
[12] A. Karamanov, M. Pelino, Sinter-crystallisation in the diopside–albite system: Part I. Formation of induced crystallisation porosity, J. Eur. Ceram. Soc. 26 (2006) 2511–2517.
[13] A. Karamanov, M. Pelino, Induced crystallization porosity and properties of sintereds diopside and wollastonite glass-ceramics, J. Eur. Ceram. Soc. 28 (3) (2008) 555–562.
[14] A. Karamanov, I. Avramov, L. Arrizza, R. Pascova, I. Gutzow, Variation of Avrami parameter during non-isothermal surface crystallization of glass powders with different sizes, J, Non-Cryst. Solids. 358 (2012) 1486–1490.
[15] D.Caurant P.Loiseau, N.Baffieer O.Majerus, C. Fillet, Crystallization study of (TiO_2,ZrO_2)-rich SiO_2-Al_2O3-CaO glasses. Part II. Surface and internal crystallization processes investigated by differential thermal analysis (DTA), J. Mater. Sci. 38 (2003) 853–864.
[16] C.L. Lo, J.G. Duh, B.S. Chiou, Low temperature sintering and crystallisation behaviour of low loss anorthite-based glass-ceramics, J. Mater. Sci. 38 (2003) 693–698.
[17] L. Cormier, G. Calas, B. Beuneu, Structural changes between soda-lime silicate glass and melt, J. Non-Cryst. Solids 357 (3) (2011) 926–931.
[18] I. Gutzow, R. Pascova, A. Karamanov, J. Schmelzer, The kinetics of surface induced

sinter crystallization and the formation of glass-ceramic materials, J. Mater. Sci. 33 (1998) 5265–5273.
[19] J. L. Amorós, E. Blasco, Transmisión de Calor en la Industria Cerámica, Castellón, Spain, 2019.
[20] E.A. Giess, J.P. Fletcher, L.W. Herron, Isothermal sintering of cordierite-type glass powders, J. Am. Ceram. Soc. 67 (1984) 549–552.
[21] R.K. Bordia, R. Raj, Analysis of sintering of a composite with a glass or ceramic matrix, J. Am. Ceram. Soc. 69 (1986) C55–C57.
[22] H.E. Exner, E.A. Giess, A stereology-based equation for isotropic shrinkage during sintering by viscous flow, Proc. Round Table on Sintering, Herzeg-Novi (1989) 73–79.
[23] C. Lara, M.J. Pascual, A. Durán, Glass-forming ability, sinterability and thermal properties in the systems RO–BaO–SiO2 (R = Mg, Zn), J. Non-Cryst. Solids. 348 (2004) 149–155.